Gas outflow and dust transport of comet 67P/Churyumov–Gerasimenko

Ian-Lin Lai,[1]* Wing-Huen Ip,[1,2,3] Cheng-Chin Su,[4] Jong-Shinn Wu,[4] Jui-Chi Lee,[5] Zhong-Yi Lin,[2] Ying Liao,[6] Nicolas Thomas,[6] Holger Sierks,[7] Cesare Barbieri,[8] Philippe Lamy,[9] Rafael Rodrigo,[10,11] Detlef Koschny,[12] Hans Rickman,[13,14] Horst Uwe Keller,[15] Jessica Agarwal,[7] Michael F. A'Hearn,[16,17] Maria Antonella Barucci,[18] Jean-Loup Bertaux,[19] Ivano Bertini,[20] Steven Boudreault,[7] Gabriele Cremonese,[21] Vania Da Deppo,[19] Björn Davidsson,[22] Stefano Debei,[23] Mariolino De Cecco,[24] Jakob Deller,[7] Sonia Fornasier,[18] Marco Fulle,[25] Olivier Groussin,[9] Pedro J. Gutiérrez,[26] Carsten Güttler,[6] Marc Hofmann,[7] Stubbe F. Hviid,[6,27] Laurent Jorda,[9] Jörg Knollenberg,[27] Gabor Kovacs,[7] J.-Rainer Kramm,[7] Ekkehard Kührt,[27] Michael Küppers,[28] Luisa M. Lara,[26] Monica Lazzarin,[8] Josè J. Lopez Moreno,[27] Francesco Marzari,[8] Giampiero Naletto,[29] Nilda Oklay,[7] Xian Shi,[7] Cecilia Tubiana[7] and Jean-Baptiste Vincent[7]

Affiliations are listed at the end of the paper

ABSTRACT

Because of the diurnal thermal cycle and the irregular shape of the nucleus, gas outflow of comet 67P/Churyumov–Gerasimenko could be highly anisotropic as indicated by the colliminated dust jet structures on the sunlit side. Based on the OSIRIS imaging observations of the outgassing effect, a simple model of surface sublimation can be constructed by taking into account the dependence on the solar insolation. With preliminary information on the time variability of the global gas production rate, a sequence of gas coma models can be generated at different epochs before and after perihelion. We also investigate different patterns of dust particle dynamics under the influences of nuclear rotation and gas drag. From these considerations, a consistent picture of the spatial distribution of dusty materials across the surface of comet 67P as it moves around the perihelion can be developed. It is found that because of the redeposition of the ejected dust from the Southern hemisphere to the Northern hemisphere during the southern summer season the Hapi region could gain up to 0.4 m while the Wosret region would lose up to 1.8 m of dust mantle per orbit.

Key words: methods: numerical – comets: general – comets: individual: comet 67P/Churyumov–Gerasimenko.

1 INTRODUCTION

The European Space Agency's Rosetta spacecraft has followed the target comet 67P/Churyumov–Gerasimenko (67P thereafter) since arrival in 2014 August. The close-up observations of the coma activities and surface morphology by the remote-sensing instruments and a suite of in situ experiments as the comet moved around its perihelion point provided a wealth of information on the basic properties of the sublimation-driven erosion of this short-period comet (Keller et al. 2015; Sierks et al. 2015; Vincent et al. 2015). Of particular importance is the transport of dust material across the nucleus surface as it has significant effects on the short-term and long-term evolution of the outgassing behaviour. In the early development of the dust mantle model (Brin & Mendis 1979; Houpis, Mendis & Ip 1985), it was suggested that the gradual growth of an insulating dust layer composed of large non-escaping solid grains on top of the pristine water ice zone will reduce the sublimation rate until total choke-off (Jewitt et al. 2004). The actual picture of surface evolution could be much more complicated.

Moehlmann ([1994](#)) discussed the lateral transport of dust grains from one part of the nucleus surface to the other parts by executing ballistic orbits. It was proposed that inactive regions can be covered by non-volatile dust particles of cm-size or greater ejected from some source regions. In the interpretation of the surface geomorphology of comet 103P/Hartley 2, Steckloff & Jacobson ([2016](#)) and Hirabayashi, Scheeres & Chesley ([2016](#)) examined the scenario of ballistic transport via surface avalanches or dust grain ejection from active zones. Based on the imaging data from the OSIRIS scientific camera (Keller et al. [2007](#); Sierks et al. [2015](#)) during the early phase of the Rosetta mission, Thomas et al. ([2015](#)) investigated how the dust particles could be redistributed across the nucleus surface as a consequence of such airfall process. From model calculations with the gravitational field determined by the mass and real shape of comet 67P, these authors showed how non-volatile grains emitted at different initial speeds (below or close to the escaping threshold of 1 m s^{-1}) in a coordinate system corotating with the nucleus can have different patterns of re-impact points. It was found that dust particles emitted from the Hapi region with initial speed of $v_i \sim 0.1$ ms^{-1} will immediately fall back to the source region after lift-off, the re-impact points will disperse to wider areas as v_i increases. An initial speed of about 0.7 ms^{-1} will yield a global regolith coverage. Larger v_i values will lead to higher escape rate and hence less and less fall back.

From the estimate of total mass-loss of $2.7 \pm 0.4 \times 10^9$ kg, Bertaux ([2015](#)) suggested that the surface layer of comet 67P could be eroded by as much as 1.0 ± 0.5 m per orbit. This value is compatible with average mass-loss rate estimated for periodic comets (Sekanina [2008](#)). On the other hand, Keller et al. ([2015](#)) discussed the possible enhanced heating of the neck region between the two lobes and the possibility of mass erosion of the order of 10 m in the south side of the nucleus which could lead to substantial mass transport from the south to the north. With focus on the northern summer season during the initial phase of the Rosetta mission when the Hapi region received maximum solar radiation and was the dominant source region, Thomas et al. ([2015](#)) estimated that with a total mass-loss rate of about 4×10^9 kg per orbit, a loose regolith layer of about 0.5 m thickness could be built up each time the comet passed the perihelion. Because the dust and gas production rates both reached peak values at perihelion and shortly afterward at which time the Southern hemisphere where Wosret, Sobek, Anhur, Geb and Bes are located was subject to intense solar heating, the dust mantle building process should be most active at that time. The Rosetta imaging observations showed that, unlike Hapi, the surfaces of these above-mentioned southern provinces are relatively free of smooth material (El-Maarry et al. [2016](#); Ip et al. [2016](#); Lee et al. [2016](#)). It is therefore important to include the dust dynamics and corresponding ballistic transport in the later phase of the Rosetta mission to the general consideration of the airfall process so that the unique surface features of comet 67P can be understood better.

The paper is structured as follows. In Section 2, we will describe several components of our model calculations. These include the solar illumination effect on surface sublimation as indicated by the Rosetta measurements, the seasonal effect, which partly controls the north–south dichotomy of the outgassing phenomena, and the time variation of the gas production rates according to the preliminary Rosetta observations. The dynamics of dust grains in the coma outflows will be analysed in Section 3, in which a numerical description of the gravitational potential field distribution of the comet nucleus is given. This is followed by the formulation of the trajectory calculations of dust grains of different sizes. The airfall process
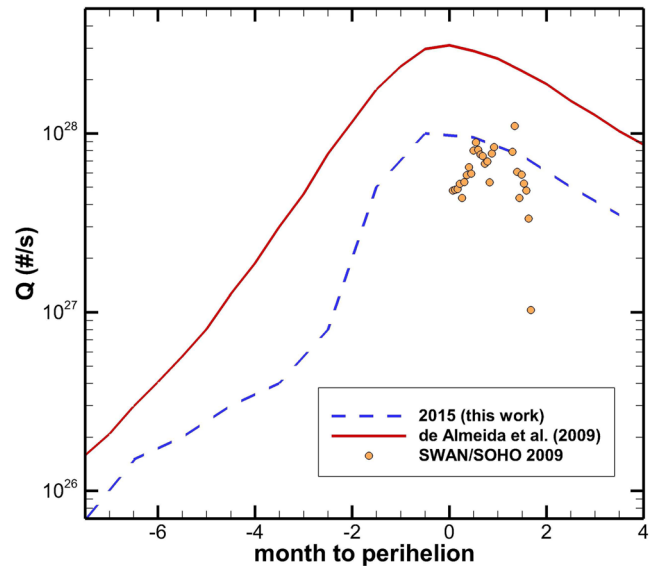

Figure 1. A schematic description of global gas production rates Q for different periods of time before and after perihelion according to de Almeida et al. ([2009](#)), Bertaux ([2015](#)) and the preliminary results from the MIRO microwave spectrometer experiment on Rosetta (Biver et al. private communication).

associated with erosion sublimation and dust mantle buildup as comet 67P moves around the sun is addressed in Section 4. Summary and discussion are given in Section 5.

2 GAS COMA DEVELOPMENT

2.1 The global outgassing rates

The gas production rate (Q) of 67P as a function of time and heliocentric distance has been monitored by ground-based observations before the Rosetta encounter. From a compilation of the estimated Q values within 2 au to perihelion from different returns, de Almeida et al. ([2009](#)) produced a radial dependence of $Q \sim Q_{dA}(r/q)^{-7}$ pre-perihelion and $Q \sim Q_{dA}(r/q)^{-3.3}$ post-perihelion with $q = 1.25$ au and $Q_{dA} = 3 \times 10^{28}$ H$_2$O molecules s^{-1}. The SWAN Lyman α photometer onboard SOHO measured a peak value of $Q = 1.5 \times 10^{28}$ H$_2$O s^{-1} near perihelion for the 2002 return but a smaller peak value of about 9×10^{27} H$_2$O molecules s^{-1} at 20 d after perihelion for the 2009 return (Bertaux [2015](#)). Preliminary results from the MIRO observations on Rosetta indicate that the pattern of outgassing process and gas production rate of 67P during the 2015 return could be similar to the SWAN values in 2009 (Biver et al. private communication) (see Fig. [1](#)).

2.2 The solar illumination effect

The outgassing effect of comet 67P is characterized by two important aspects. The first one has to do with the remarkable north–south dichotomy. Because of the 52° tilt of the rotational axis of the nucleus to the ecliptic plane (Sierks et al. [2015](#)), only the Northern hemisphere was illuminated on the inbound leg until equinox in 2015 May. Until this point, the Hapi region was the most important source region of gas and dust (Biver et al. [2015](#); Haessig et al. [2015](#); Lara et al. [2015](#); Lin et al. [2015](#); Sierks et al. [2015](#)). The Southern hemisphere in shadow was found to emit CO$_2$, CO and other gas molecules of volatility higher than that of water (Bockelee-Morvan

et al. 2015; Haessig et al. 2015). The water ice sublimation was gradually turned on in the Southern hemisphere when it was sunlit in 2015 May and reached the maximum level at perihelion while the outgassing rate subsided in the Hapi region. This brings to mind the second essential feature that is termed 'solar insolation effect'. That is, the nucleus surface can emit coma gas with sublimation rate depending mainly on the solar zenith angle (θ). Such solar illumination effect in ice sublimation was analysed quantitatively by Cowan & A'Hearn (1979). More recently, the azimuthal dependence of the sublimation process was applied to the nucleus evolution of the sun-grazing comet C/2012 S1 ISON by Steckloff et al. (2015). In the case of comet 67P, Bieler et al. (2015) found similar effect by comparing theoretical models with the ROSINA-COPS measurements. This also means that a strong day–night asymmetry always exists in the inner coma of comet 67P.

From the orientation of the nucleus (Sierks et al. 2015) and the shape model obtained by the OSIRIS imaging camera experiment (Jorda et al. 2016), the diurnal variation of the solar illumination can be determined. The sublimation rate on a certain facet is assumed to be given by $Z \sim \cos\theta$. As the nucleus rotates around, each sunlit facet will experience time variation of the solar radiation flux and heating effect. In principle, the surface sublimation rate should be the highest at local noon ($\theta \sim 0°$) and taper off to zero as θ increases from $0°$ to $90°$. To speed up the calculation, the average value ($\langle\cos\theta\rangle$) of the solar zenith angles on the sunlit side over one rotation is computed for each facet from which an average sublimation rate is generated by using $\langle Z \rangle \sim \langle\cos\theta\rangle$.

The next step is to estimate the surface temperature of each facet which can be derived from the following energy balance equation. The following expression is for the ith facet (Weissman & Kieffer 1982):

$$\frac{S_\odot(1 - \alpha_H)\langle\cos\theta\rangle_i}{R_H{}^2} = \epsilon\sigma T^4 - L\langle Z\rangle_i. \tag{1}$$

In the above equation, α_H is the albedo ($\alpha_H = 0.4$), $S_\odot$ is the solar constant at 1 au, R_H is the heliocentric distance of the comet, ϵ is the infrared (IR) emissivity ($\epsilon = 0.9$), σ is the Stefan–Boltzmann's constant, L is the latent heat and $\langle Z\rangle$ is the local sublimation rate. We assume the initial gas temperature is equal to surface temperature. In the regions in permanent shadow, we set the temperature $T = 40$ K as measured by the MIRO experiment on Rosetta (Schloerb et al. 2015). The water molecules emanate from the surface of the comet with a half-Maxwellian velocity distribution in which gas dynamics will be followed by the DSMC (Direct Simulation Monte Carlo) method. The DSMC code, PDSC++, is a general-purpose parallel 2D/2D-axisymmetric/3D DSMC code using unstructured grid, which is developed by Wu's group. Some important features of the PDSC++ include hybrid unstructured mesh, variable time-step scheme (Wu, Tseng & Wu 2004), transient adaptive sub-cell method (Su et al. 2010), unsteady simulation (Cave et al. 2008), domain re-decomposition, automatic steady state detection scheme, parallel computing technique and chemical reaction based on total collision energy model (Lo et al. 2015). It also has been applied to the rare gas flows of cometary comas (Finklenburg et al. 2014; Lai et al. 2016; Liao et al. 2016; Marschall et al. 2016). In our DSMC calculation, we neglect the effect of dust particles in the gas flow in accordance with other DSMC codes (Tenishev, Combi & Rubin 2011).

2.3 The seasonal effect

Fig. 2 shows the spatial variations of the $\langle\cos\theta\rangle$ value between 0 and 0.65 on the first day of each month in 2015. The gradual southward movement of the sunbelt with the arrival of equinox on 2015 August 15 can be clearly seen. With the gradual illumination of the Southern hemisphere, the solar heating reaches maximum at perihelion. It is noted that the time evolution of the sunlit zone is consistent with the pattern of dust jets emitted from the nucleus surface as observed by the OSIRIS science camera experiment. In addition to the sunlit condition, the effective solar radiative flux will vary with the heliocentric distance R_H (see equation 1). The actual ejection rate (and redeposition rate) of dust particles would necessarily depend on the corresponding gas sublimation rate and how much dust can be lifted off.

3 DUST TRAJECTORY CALCULATIONS

3.1 Gas coma outflow models

For the gas outflow, our approach in agreement with the MIRO measurements (Biver et al. private communication) is to prescribe a fraction of about 85 per cent to the total gas production from the dayside and another fraction of about 15 per cent with a uniform sublimation rate to the whole surface (Keller et al. 2015). The partition of the dayside sublimation rate is further assigned by the relative values of $\langle Z \rangle$ in individual facets. If the total gas production rate is $Q(t)$ at time t, this means that we have basically an isotropic component of coma outflow with total gas production $Q_2 = 0.15Q(t)$ and a strong anisotropic component of gas outflow with $Q_1 = 0.85Q(t)$ from the dayside.

Fig. 3 compares the DSMC 3D coma outflow patterns of 2015 January and 2015 August, respectively, showing the switching of the anisotropic component from north to south. Note the increase of the flow speed from 600 to 750 m s^{-1} in this time interval. The numerical results in three dimensions from the DSMC model calculations will allow the next step of simulation of launching dust grains from the nucleus surface.

3.2 The gravitational field of 67P

In a rotating coordinate system attached to the cometary body, the acceleration of a dust particle can be written as

$$\frac{d\boldsymbol{v}}{dt} = \boldsymbol{a}_{\text{drag}} + \boldsymbol{a}_{\text{g}} + \boldsymbol{a}_{\text{centrifugal}} + \boldsymbol{a}_{\text{Coriolis}}$$
$$= \boldsymbol{a}_{\text{drag}} + \boldsymbol{a}_{\text{g}} - \boldsymbol{\omega} \times (\boldsymbol{\omega} \times \boldsymbol{r}) - \boldsymbol{\omega} \times \boldsymbol{v}_{\text{dust}}, \tag{2}$$

where $\boldsymbol{a}_{\text{drag}}$ is the acceleration of dragging force, $\boldsymbol{a}_{\text{g}}$ is the effect of gravitational acceleration, $\boldsymbol{\omega} = 2\pi/P$, the rotation period of 67P which is 12.4 h and $\boldsymbol{r}$ is the distance from the rotational centre of the comet. The gravity is calculated by constructing a simplify model based on version SHAP5 (Jorda et al. 2016) of the shape model. To do this, we discretized the volume in 359419 volume elements. The gravitational acceleration a_{g} of a small element exhibited at any point in the 3D space can be written as,

$$\boldsymbol{a}_{\text{g}} = G\rho \sum \frac{\boldsymbol{r}_i \triangle V_i}{|\boldsymbol{r}_i^3|} \tag{3}$$

where G is the gravitational constant, $\triangle V_i$ is the volume of the ith elements, r_i is the distance from the location to the centre of this element, and we assume a homogeneous bulk density of $\rho = 532$ kg m^{-3} (Jorda et al. 2016). Because of the irregular shape, there are some local positions with lower gravitational potential on the surface of the head, neck and body. The gravitational potential field distribution was calculated by integration of the gravitational
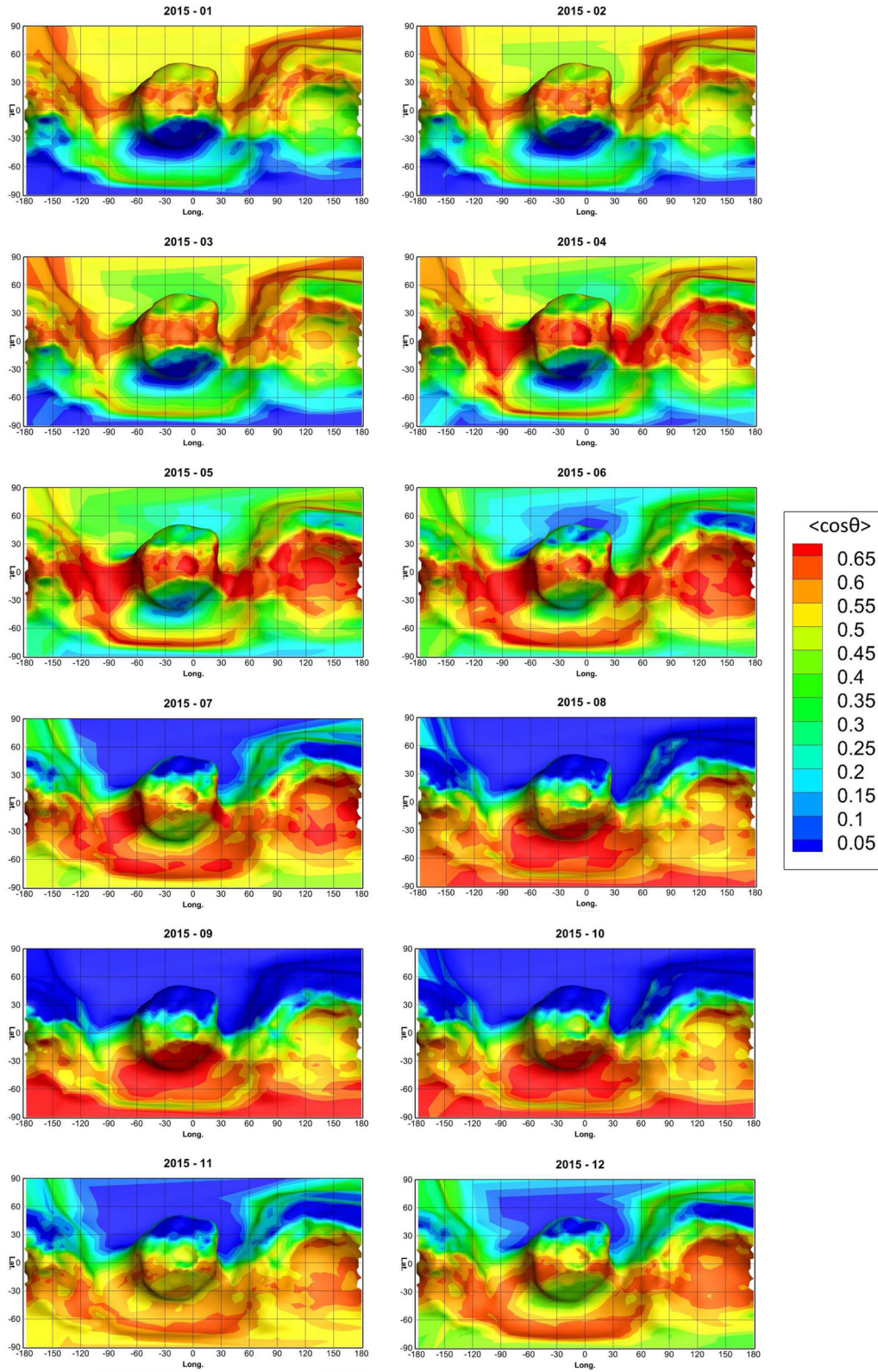
Figure 2. Temporal and spatial variations of the average values of the sunlit angle parameter $\langle \cos\theta \rangle_i$ from 2015 January to December according to the cometary shape model provided by the OSIRIS science camera experiment (Jorda et al. 2016).
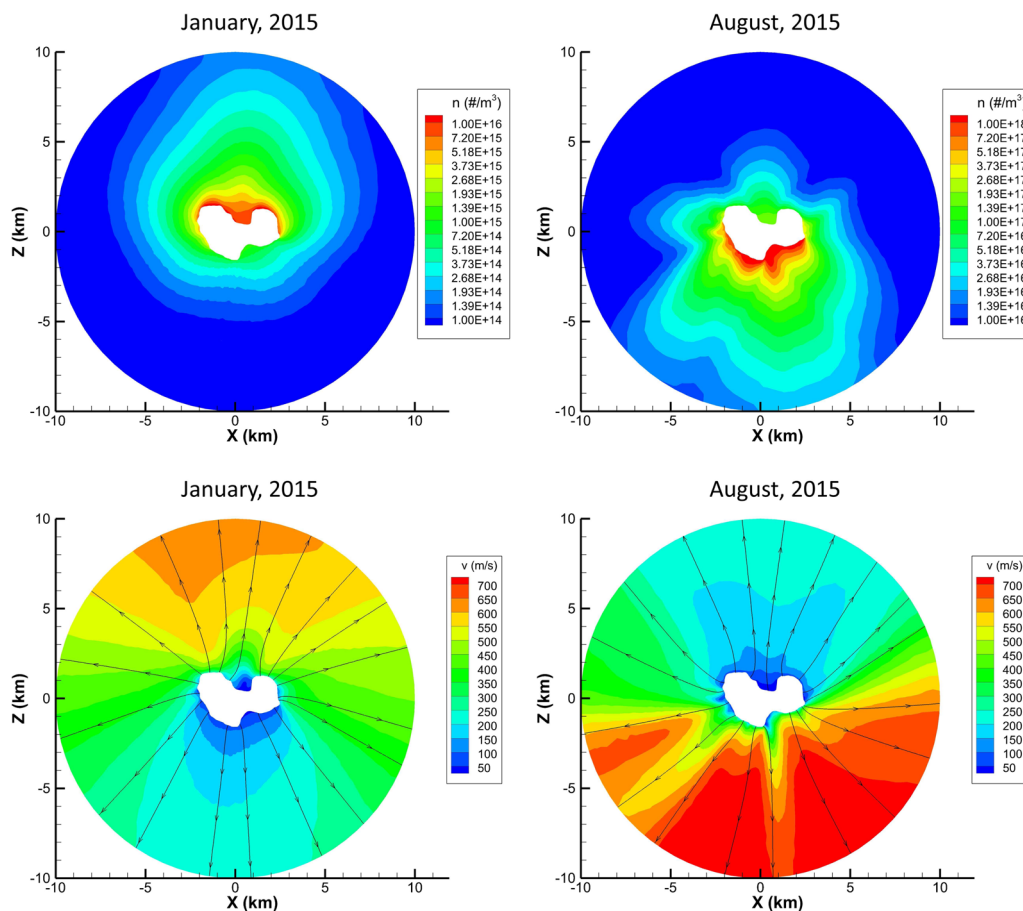
Figure 3. A comparison of the coma gas outflow pattern in 2015 January (left) and August (right), respectively. Upper panels: the H_2O number density distributions; lower panels: the velocity distributions and gas streamlines. The total H_2O production rates are assumed to be $Q(1/2015) = 7 \times 10^{25}$ molecules s^{-1} and $Q(8/2015) = 1.0 \times 10^{28}$ molecules s^{-1}, respectively, according to the preliminary results of the MIRO measurements (Biver et al. private communication).
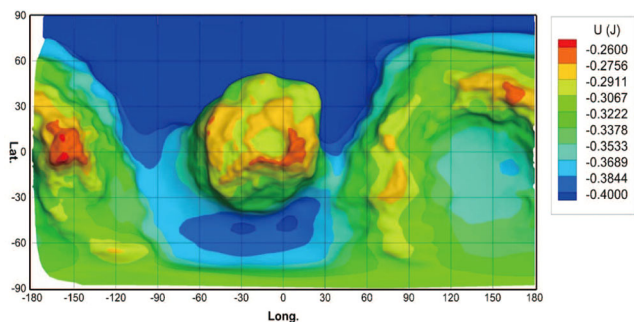
Figure 4. A Mercator projection of the gravitational potential (U) of comet 67P.

acceleration field. Fig. 4 shows only the potential of gravity on the nucleus surface and does not include the rotational potential.

3.3 The dust motion

We consider the dust grain as a spherical icy particle with a cross-section $\sigma_d = \pi a^2$, where a is the grain radius. The acceleration of the dust particle due to the drag force can be written as (Marschall et al. 2016)

$$\boldsymbol{a}_{\mathrm{drag}} = \frac{1}{2} C_d \sigma_d (\boldsymbol{v}_{\mathrm{gas}} - \boldsymbol{v}_{\mathrm{dust}}) \left| \boldsymbol{v}_{\mathrm{gas}} - \boldsymbol{v}_{\mathrm{dust}} \right| \rho_{\mathrm{gas}}, \tag{4}$$
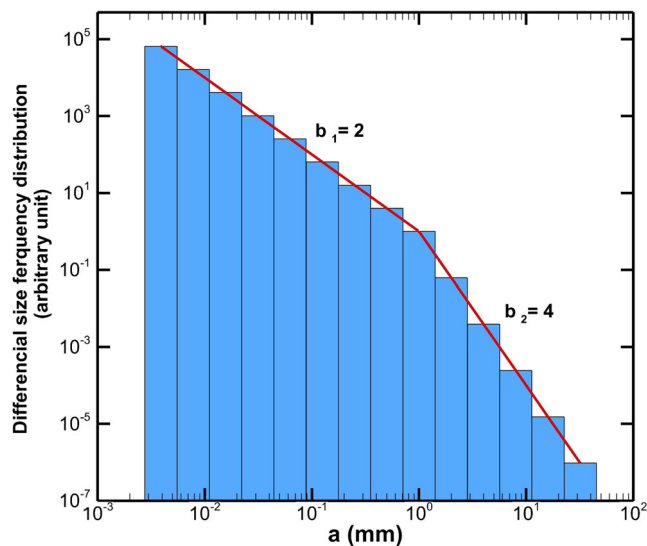

Figure 5. An illustration of the dust particle size distribution and the size binning adopted in the present study.
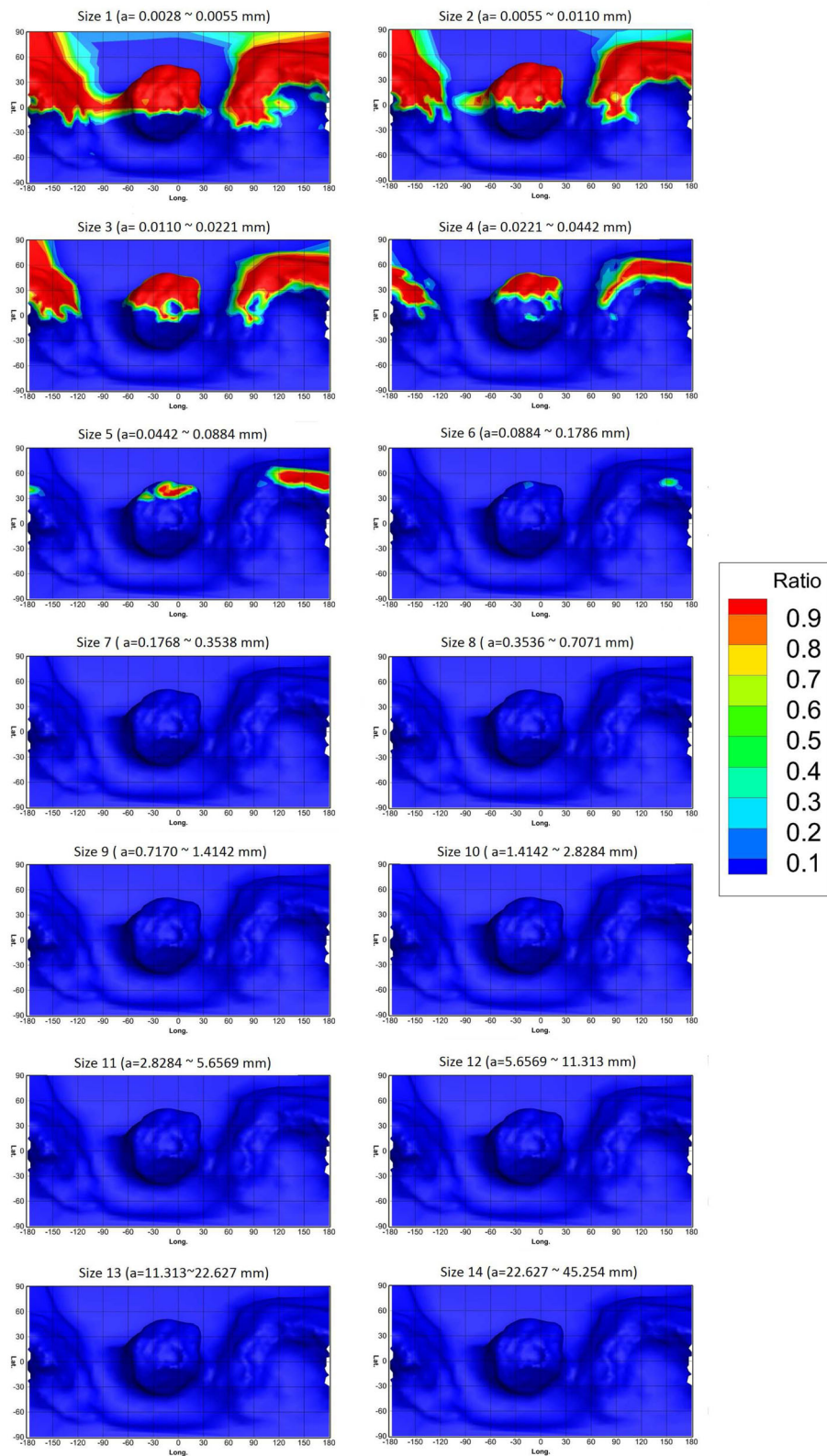
Figure 6. The temporal and spatial variations of the escape efficiency (0 for no escape and 1 for total escape) of cometary dust particles of different median sizes ranging from 3 nm (the median value in size bin no. 1) to 3 cm (the median value in size bin no. 14) in 2015 January.
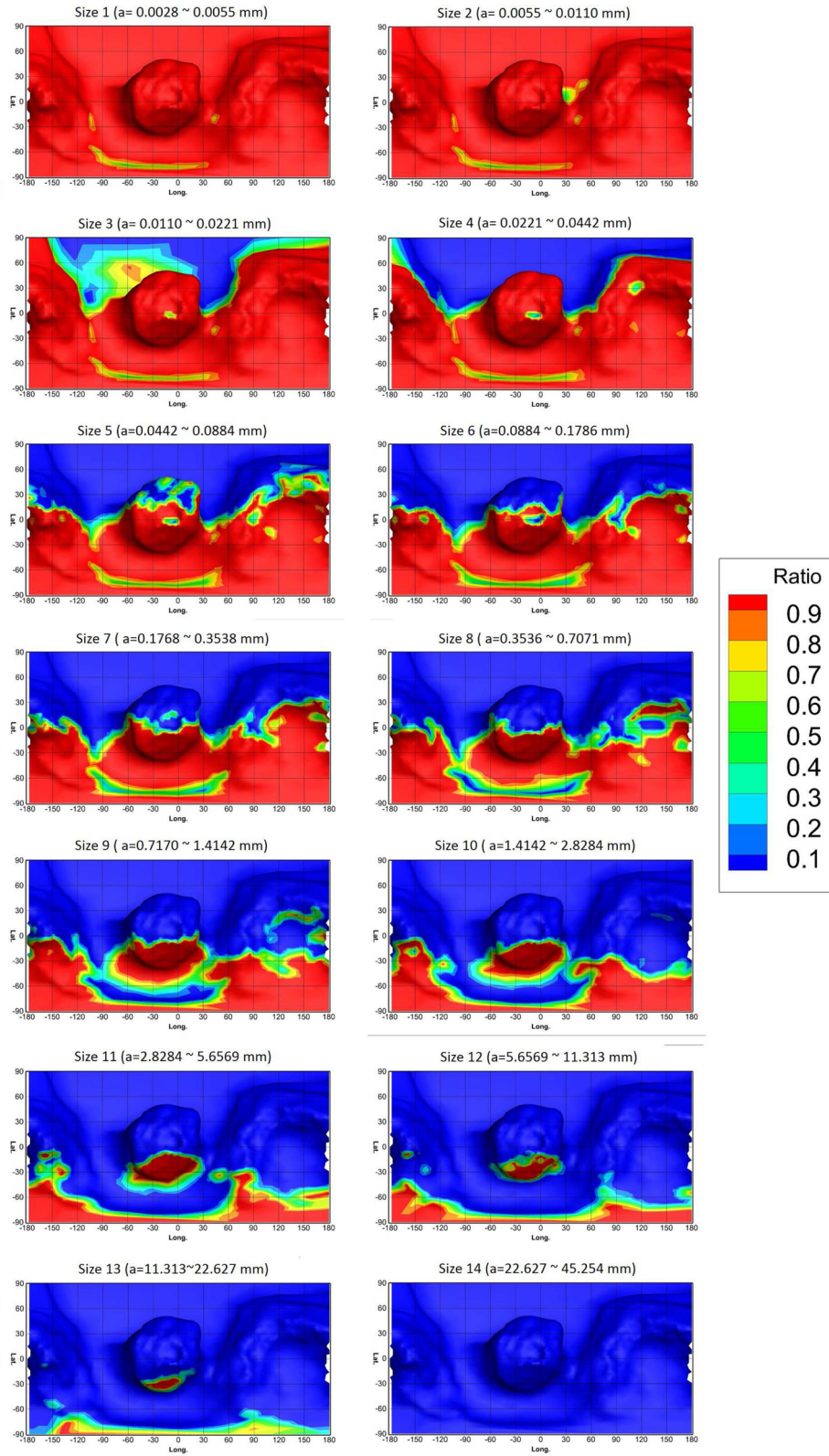
Figure 7. Same as Fig. 6, but for 2015 August.

where $\boldsymbol{v}_{\text{gas}}$ is the velocity of the local gas flow, $\boldsymbol{v}_{\text{dust}}$ is the velocity of dust particle, ρ_{gas} is the mass density of the local gas flow and C_{d} is the drag coefficient that can be defined as (Marschall et al. 2016),

$$C_{\text{d}} = \frac{2s^2 + 1}{\sqrt{\pi}s} + \frac{4s^4 + 4s^2 - 1}{2s^4} erf(s) + \frac{2\sqrt{\pi}}{3s}\sqrt{\frac{T_{\text{dust}}}{T_{\text{gas}}}}, \tag{5}$$

$$s = \frac{|\boldsymbol{v}_{\text{gas}} - \boldsymbol{v}_{\text{dust}}|}{\sqrt{\frac{2kT_{\text{gas}}}{m_{\text{gas}}}}}, \tag{6}$$

where T_{gas} is the temperature of the gas, T_{dust} is the temperature of the dust (assume $T_{\text{gas}} = T_{\text{dust}}$), and no specular reflection of the gas molecules at impact with the dust grains because of the porous structure of the grain surface.

Because of differences in size and mass, dust grains with radii from sub-micron to cm would experience different gravitational force and viscous gas drag effects. To begin with, the dust size distribution is assumed to follow a power-law distribution $dn/da \sim a^{-b}$, where b is the power-law index. As illustrated in Fig. 5, the power-law distribution has a break at $a = 1$ mm with $b_1 = 2$ for $a < 1$ mm and $b_2 = 4$ for $a > 1$ mm, according to the observations of the dust coma of comet 67P (Fulle et al. 2010, 2016). In our study, this size distribution is divided into 14 size bins in logarithmic scale between 2.8 µm and 4.5 cm. See Lin et al. (2016) for examples of velocity profiles of dust grains with different sizes.

For each size bin, 400 000 particles are placed randomly over the whole nucleus surface for the specific time under consideration. Because of the finite size of the facets, test particles emitted from the same facet could have somewhat different trajectories. In the airfall scenario of Thomas et al. (2015), an important parameter is the escape efficiency of the test particles in different size bins. Figs 6 and 7 illustrate the distribution of this parameter across the nucleus surface of comet 67P for different dust sizes in 2015 January and August, respectively. As can be seen in Fig. 6, during the northern summer the escape flux of large particles ($a \sim 0.1$ mm) would be limited even in the regions with strong solar illumination. It is however, possible that in some localized areas characterized by collimated jet structures mm-sized dust would be ejected (Lara et al. 2015; Lin et al. 2015, 2016). Dust particles that are accelerated to beyond the escape velocity will move into the expanding dust coma and dust tail and eventually become a part of the interplanetary dust medium.

In Fig. 7, we see that at the peak of the gas production rate near perihelion passage in 2015 August dust grains up to 10 mm can be ejected from the nucleus surface. It is therefore likely that a population of cm-sized grains would have been injected into the dust coma in this time period under normal condition. On the occasions of large outbursts as often seen between 2015 July and September, that might have been generated by thermal stress and/or cliff collapse (Vincent et al. 2015, 2016), particles of even metre-size could be ejected (Pajola et al. 2015). The validity of this approximation depends on the radiative cooling process of the nucleus surface as examined by Sekanina (1988, 1992).

4 EROSION VERSUS BUILDUP OF REGOLITH LAYERS

4.1 The ballistic transport of the dusty material

The return flux of the non-escaping dust grains and re-distribution among different facets on both the dayside and nightside will depend on the exact trajectories of individual particles. Fig. 8 illustrates the
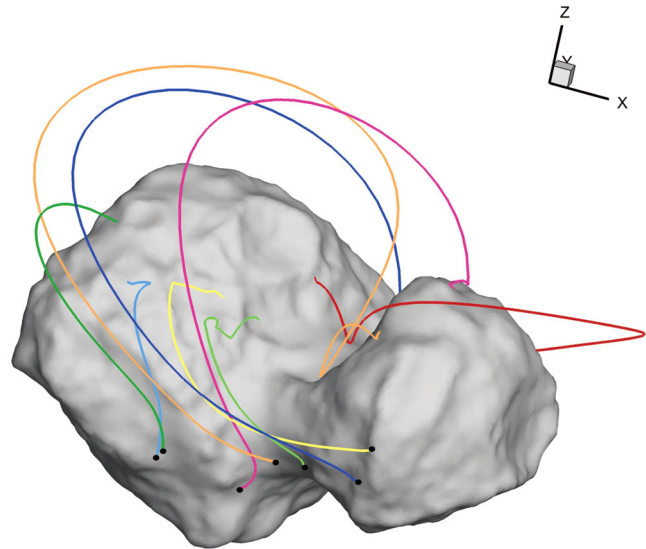

Figure 8. Examples of the trajectories of non-escaping dust particle across the nuclear surface. The black spots show the launching points of the dust particles.

ballistic motion of some non-escaping dust grains across the nucleus surface. In the present scenario, it is assumed that the particles after surface impact will rebound (as in the case of the Philae lander) in random direction because the nucleus surface should be relatively rough at mm scale. In any event, the case of re-bounce in the original impact direction has been tested and no major difference was found in the results. It is also assumed that the ejection speed is 50 per cent of the impact speed to account for inelastic collision. As shown, the hopping distances of the rebounding particles are generally small and the final residence locations are usually in the neighbouring facets around the first impact sites.

4.2 The dust mantle building

If the sublimation rate $\langle Z \rangle$, escape efficiency and global map of re-impact points of different size bins are computed for each facet according to the above-mentioned numerical procedure, we would be in the position to estimate the mass erosion rate and mass accretion rate of the regolith layers in various regions of the nucleus surface. A key step is to give a weighting factor to each launched test particle in our simulation such that such a simulated macroparticle can represent the mass of many dust grains in the real situation. The approach we follow is to sum up the number of emitted particles in different bin sizes to reconstruct a pseudo-size frequency distribution (dn/da) for each facet. We note that the pseudo-SFDs so obtained might not be exactly the same as the original SFD plotted in Fig. 5 because of the nature of our Monte Carlo model calculation. The integral mass flux contained in this ensemble of dust particles is assumed to be proportional to the sublimation rate of the facet in question. The differential mass flux contained in individual size bins can be computed by taking into account the relative mass ratios (β_j) from size bin $j = 1$–14. Finally, the mass escape rate represented by each macro-particle in the jth size bin emitted from the ith facet with sublimation rate $\langle Z \rangle_i$ and a cross-section A_i is obtained by $W_{ij} = \xi \beta_j A_i \langle Z \rangle_i / K_{ij}$, where ξ is the dust-to-gas mass ratio and K_{ij} is the number of ejected test
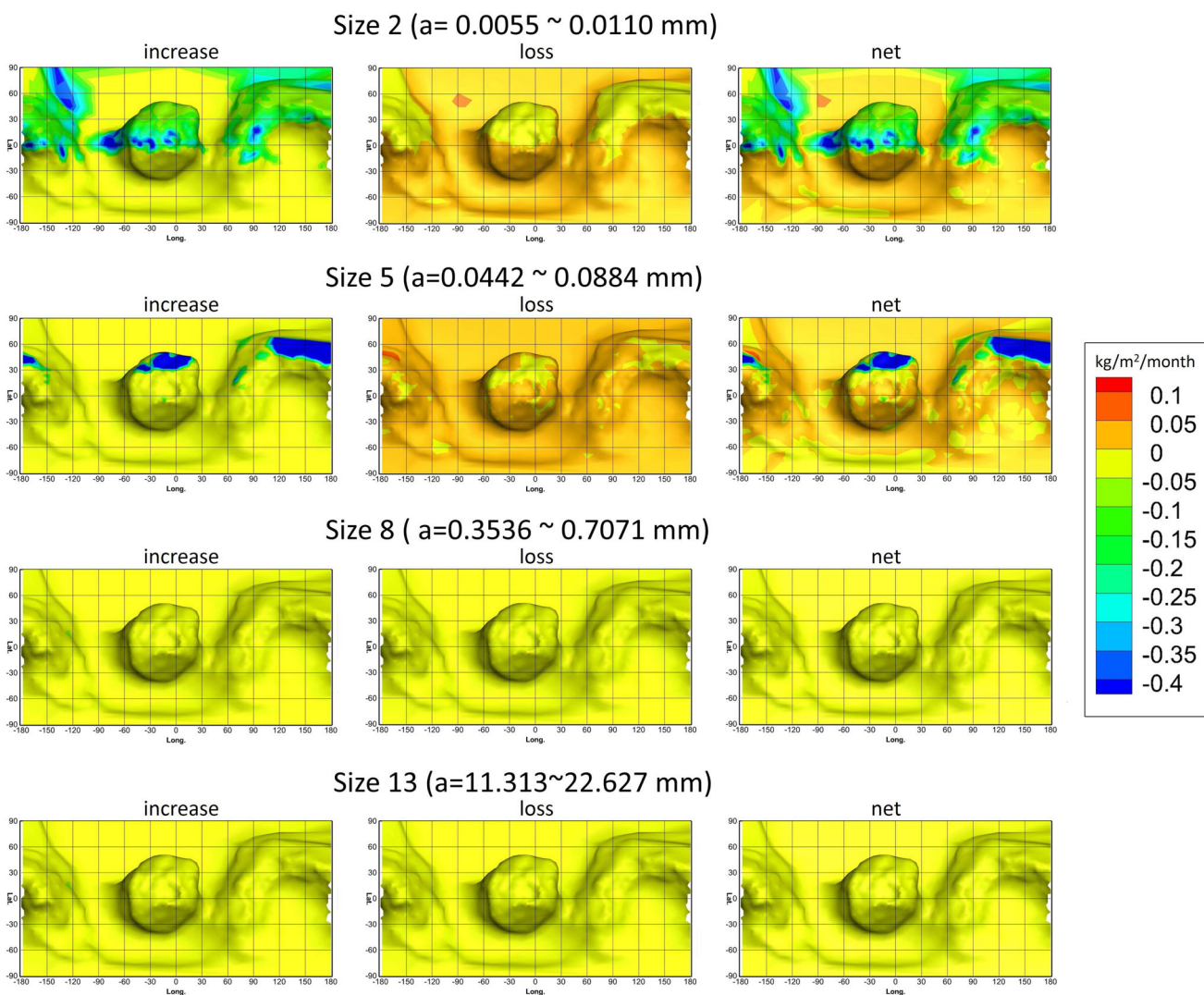
Figure 9. Examples of the spatial distributions of the mass-loss rate, mass influx and net mass change rate (in unit of kg m^{-2} per month) of several selected dust sizes in 2015 January.

particles of the jth size bin. Following Fulle et al. (2016), we assume $\xi = 6$.

The launch of K_{ij} particles from the facet 'i' with the weighting factor W_{ij} means a mass-loss rate of $\triangle \dot{M}_{ij}(-) = \xi \beta_j A_i \langle Z \rangle_i$. The total mass-loss rate of this facet is therefore $\dot{M}_i(-) = \sum_j \triangle \dot{M}_{ij}$ by summing up contributions of dust particles in different size bins. At the same time, the impact of a macro-particle with the weighting factor $W_{i'j'}$ at the ith facet will be recorded as a mass accretion rate given by $W_{i'j'}$ and the total mass accretion rate of this facet will be given by $\dot{M}_i(+) = \sum_{i'} \sum_{j'} W_{i'j'}$. The net mass change (increase or loss) rate of the ith facet is therefore given by $\dot{M}_i = \dot{M}_i(+) + \dot{M}_i(-)$.

Fig. 9 gives snapshots of the $\dot{M}_i(-)$, $\dot{M}_i(+)$ and $\dot{M}_i$ over the nucleus surface in 2015 January. Because of the solar illumination condition, erosion sublimation occurs only above the equator. The left-hand panels for $\dot{M}_i(-)$ illustrate the hot spots of mass-loss because of sunlit condition (see Fig. 6). Only dust particles of size <0.1 mm would be ejected because of the relatively weak gas production rate of 7×10^{25} molecules s^{-1} globally. However, we

note that larger grains could be emitted at localized areas because of jet activity (Lara et al. 2015; Lin et al. 2015). The middle panels give us some idea on how the airfall effect would refill the nucleus surface with the dust emitted from the hot zones. The right-hand panels show the net result $\dot{M}_i$ identifying the Ash and Ma'at regions as the most affected by erosion sublimation ($\dot{M}_i < 0$) whereas the Hapi region as a place with mass net gain ($\dot{M}_i > 0$) even though the amount is small ($\dot{M}_i \sim 0.6$ kg m^{-2} per month).

Fig. 10 gives examples of the surface mass change rates in 2015 August. Because of the strong gas production rate, dust particles with $a \sim 10$–20 mm will be ejected from the Southern hemisphere. The dust grains in this size range do not move too far away from their source regions. The effective mass transport effect is therefore not significant (see panels for size bin 13). Instead, it is the dust population in the size range of about 0.1–1.0 mm (i.e. size bin $\sim$5– 8 in Fig. 10) that will be important in the mass transport process. The southern provinces, especially the Bes and Wosret regions, are losing mass during the perihelion passage. On the other hand, the northern provinces, Hapi region in particular, can quickly add a new
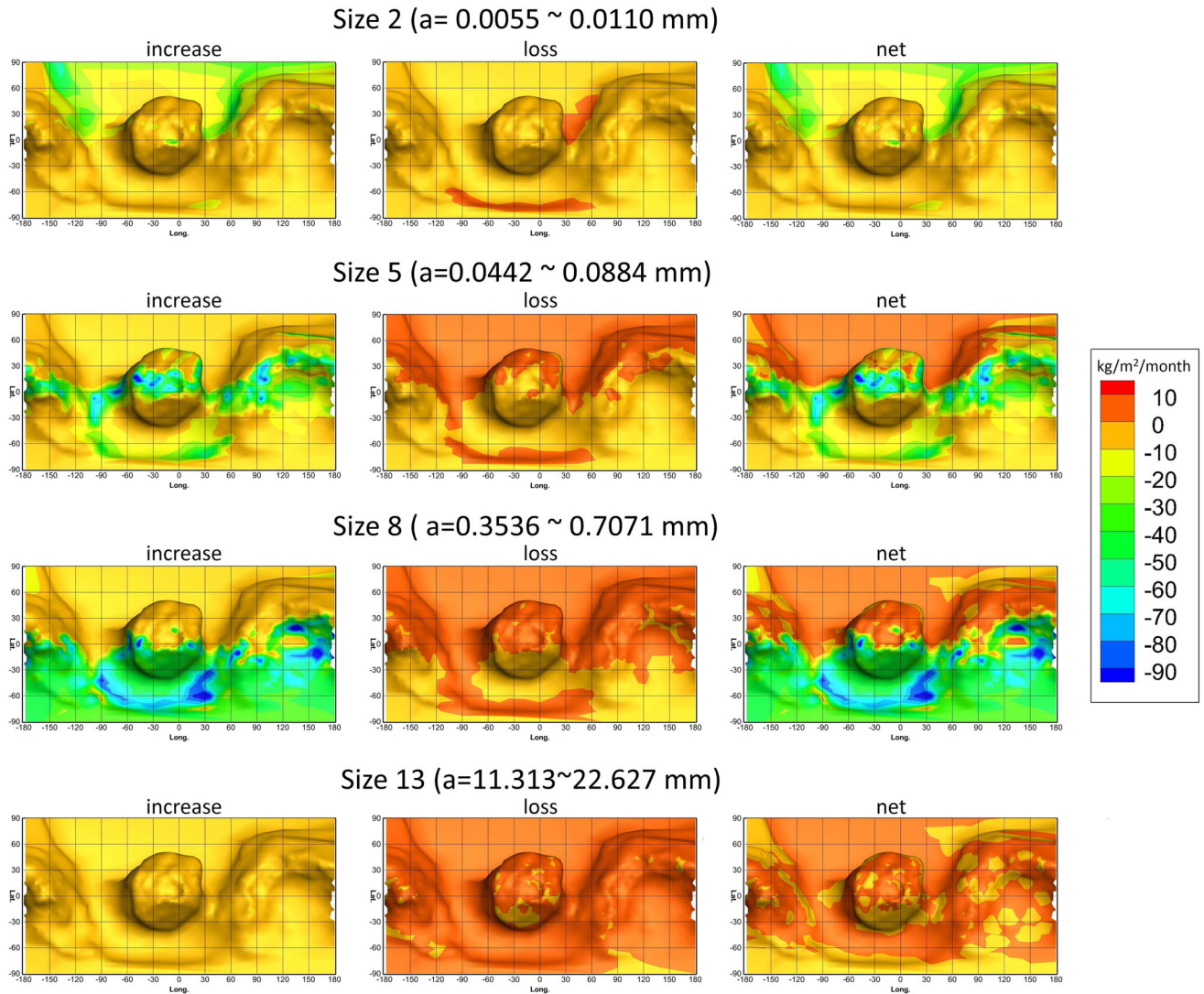
Size 2 (a= 0.0055 ~ 0.0110 mm)

Size 5 (a=0.0442 ~ 0.0884 mm)

Size 8 (a=0.3536 ~ 0.7071 mm)

Size 13 (a=11.313~22.627 mm)

Figure 10. Same as Fig. 9 but for 2015 August.

regolith layer because of the dust infall with $\dot{M} \sim 50$ kg m^{-2} per month.

5 RESULT

Fig. 11 compares the mass change over the nucleus surface in 2015 January and August, respectively. The monthly mass change is estimated by multiplying the corresponding mass change rate of each size bin with the time ($\triangle t = 30$ d) and then sum them all up. In January, the outgassing activity above the equator leads to mass-loss in most parts of the Northern hemisphere except for the Hapi region. Some of the dust ejected will be recycled (redeposition) to the Southern hemisphere that was in darkness at that time. During perihelion passage in August, the gas production rate in our model is high enough that even the isotropic background outflow discussed in Section 3 can accelerate micron-sized particles (size bin 1–3) away from the nucleus surface (see Fig. 6). As a consequence, only a patch of limited area in the Hapi region can retain mass influx of this size range.

As an approximation to the evolution of the regolith layer, we repeat the same computational procedure for all months of 2015

using the gas production rate at the beginning of each month as described in Fig. 1. The corresponding net mass changes month by month so obtained are added together to produce the cumulative mass change in global scale.

Fig. 12 shows the increase or decrease of the dust mantle obtained by dividing the cumulative mass change with the nucleus bulk density ρ of 0.53 g cm^{-3} (Jorda et al. 2016). According to our model calculation limited to the time interval between 2015 January and December, the Hapi region has net gain of dust mass with the development of an additional regolith layer of thickness of ~0.4 m (at least) in one orbit. Everywhere else except for some localized spots would lose mass. The southern side of the Bes and Wosret region appears to be subject to a high level of mass-loss.

In Fig. 13, the geomorphologies of several regions on comet 67P are compared with the numerical results. In good agreement with Thomas et al. (2015), the Hapi region is heavily covered by dust as a consequence of the airfall effect (Figs 13 a and b). However, the major dust mantle buildup is found to take place near perihelion when the outgassing activity was the strongest in the Southern hemisphere. Dust-filled regions with limited thickness of the regolith layers might exist in the top parts of Imhotep and
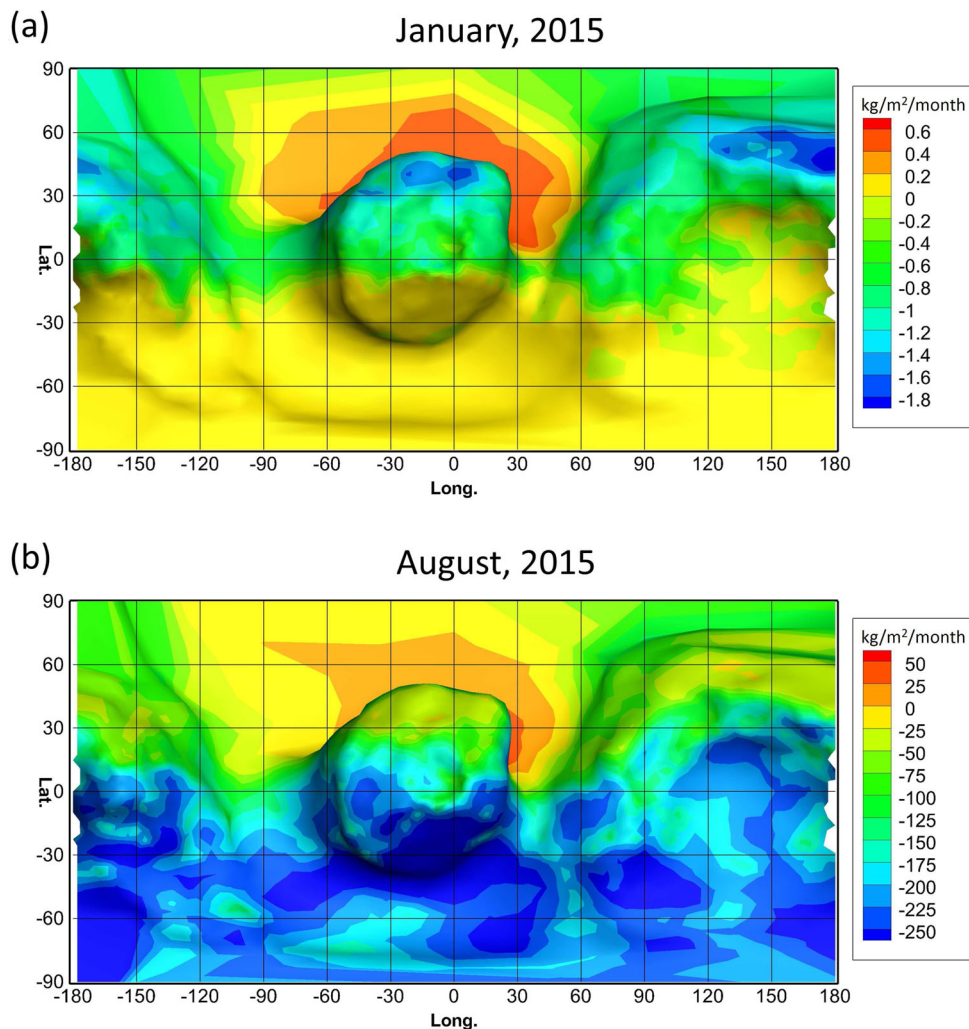
Figure 11. A comparison of the net mass gain (or loss) rates in 2015 January and August, respectively, by integrating together all 14 size bins in unit of kg m^{-2} per month.
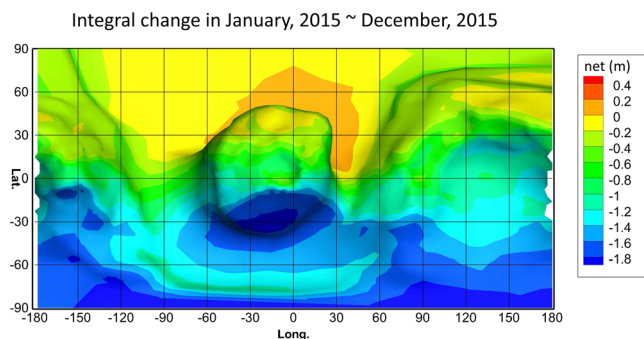

Figure 12. The integral change of thickness of the regolith layer from 2015 January to 2015 December.

Hatmeit, respectively. This conjecture appears to be supported by the OSIRIS observations (see Figs 13 c–f). Finally, the Southern hemisphere should be largely clear of dust-rich regolith layer because of the strong outgassing activity at and after perihelion (see Fig. 1). However, some localized patches in the southern neck in the vicinity of Anhur and Sobek could still harbour sand ponds. This nu-

merical result is also consistent with the observed geomorphology shown in Figs 13(g) and (h).

6 SUMMARY AND DISCUSSION

Based on the studies of the surface mass erosion and transport before and in the early phase of the Rosetta mission (Bertaux 2015; Keller et al. 2015; Thomas et al. 2015), a first-generation numerical model of the regolith growth on comet 67P is produced by integrating several key elements. These include the time profile of the water production rates derived from ground-based, space-born and Rosetta observations (de Almeida et al. 2009; Bertaux 2015; Biver et al. private communication). The peak value of the water production rate is taken to be 10^{28} molecules s^{-1} which is subject to change upon more detailed analyses (Biver et al. private communication). Following a simple solar illumination effect in the control of surface sublimation, the average value of the cosine of the solar zenith angle (θ) according to the nucleus shape model (Jorda et al. 2016) in each facet is computed and the average sublimation rate of a facet follows the relation: $\langle Z \rangle \sim \langle \cos \theta \rangle$. The global distribution of the surface sublimation rates is further divided into two components. One of the gas components is assumed to accounts
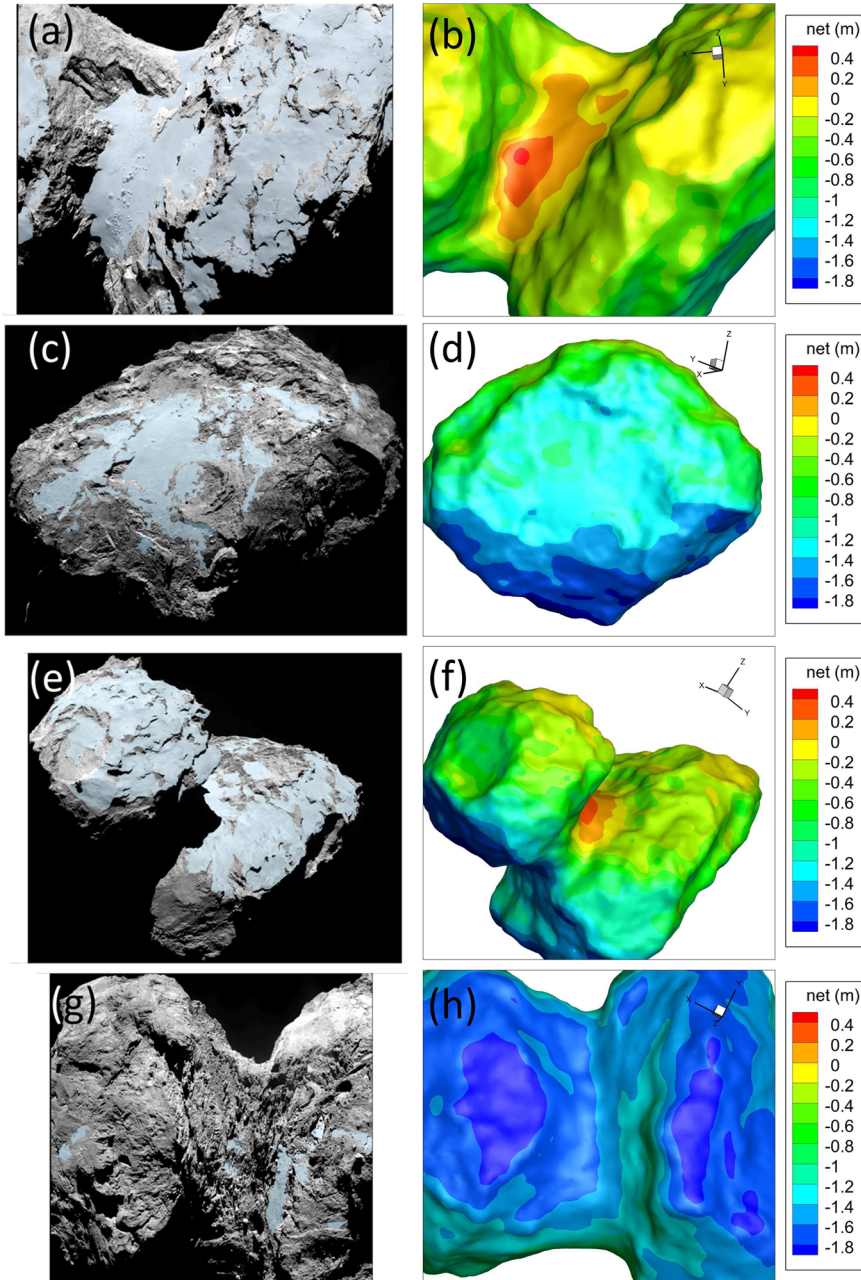
Figure 13. Comparison of the surface geomorphology with the simulation results: (a and b) Hapi; (c and d) Imhotep; (e and f) Hatmeit and (g and h) Southern hemisphere. See Table 1 for the image information.

for 85 per cent of the total gas production rate and the anisotropic gas emission pattern is determined by the cosine law. The second component, containing 15 per cent of the total gas production rate, has an isotropic gas sublimation rate that is independent of the solar zenith angle. Such partition of the gas emission rates has been indicated by the MIRO observations of the water gas coma (Biver et al. private communication).

To derive the dust production rate and the related mass transport process, we make use of the dust size frequency distributions reported by Fulle et al. (2016). Coupled with the time profile of the gas production rates, the ejection and re-impact of dust particles of different sizes can be simulated at different orbital phases of comet 67P. In the present study, the focus is on the dust mantle development in 2015. We can examine the step-by-step mass exchange

between various surface regions as the sunlit zone progresses from the Northern hemisphere to the Southern hemisphere. This model calculations show how the Hapi region could gain a new regolith with thickness of about 0.4 m at least in each orbit. The lack of wide-spread dust cover on the southern provinces like Geb and Anhur can also be understood.

There are several things to follow up in future investigations. For example, upon the availability of the 'official' gas production rate curve we would be able to produce a more accurate model with longer time coverage (to 2016, say). A deeper understanding of the sublimation process would allow a more realistic description of the parametric dependence of the gas production rates in different areas. The phenomenological relation of $\langle Z \rangle \sim \langle \cos\theta \rangle$ cannot explain well why the Hapi region was observed to be the major source region

Table 1. The images used in this study.

Figure	ImageID	Distance (km)[a]	Pixel scale (m)
13a	NAC_ 2014-08-20T01.42.54.569Z_ IDB0_ 1397549300_ F22	85.9	1.5
13c	NAC_ 2015-05-02T04.54.10.779Z_ ID30_ 1397549002_ F41	125.4	2.3
13e	NAC_ 2014-08-05T23.20.11.041Z_ IDB0_ 1397549300_ F41	123.4	2.3
13g	NAC_ 2016-01-27T17.20.08.041Z_ ID30_ 1397549000_ F22	70.4	1.3

[a]The distance between spacecraft and the centre of comet 67P.

of gas and dust jets (Lin et al. 2015; Sierks et al. 2015) when the Northern hemisphere was in sunlight. It may therefore be interesting to include self-heating (Keller et al. 2015) into the analysis even though it is outside the scope of the present study.

For future work, the effect of the diurnal outgassing behaviour should also be incorporated. In this regard, it should be mentioned that the deceleration of the dust grains by the gas outflow during their re-entry might be important in screening the returning sub-mm dust grains from reaching the north winter hemisphere near perihelion as discussed by Fulle et al. (2016). Another effect has to do with the higher and higher level of recycle of non-escaping dust grains of increasing sizes until the cutoff point where no dust particles with larger size will be lifted off from the facets. The combined effect might provide a physical mechanism in producing a flatter size distribution ($b_1 \sim 2$) for small dust grains (i.e. $b_1 \sim 2$ and $b_2 \sim 4$ as illustrated in Fig. 5) emitted from Hapi region even though the original size distribution of the dust from the source region in the Southern hemisphere should be characterized by both b_1 and b_2 being equal to 4. We plan to examine this process quantitatively in future work. Finally, violent outbursts probably triggered by explosive events or cliff collapse as discussed by Vincent et al. (2016) could potentially play an important role in mass transport if a large amount of materials is ejected. With such scenario in mind, the detailed comparison of the small geomorphological features (i.e. pits and boulders) imaged before and after perihelion would be most interesting.

ACKNOWLEDGEMENTS

REFERENCES

Bertaux J.-L., 2015, A&A, 583, A38
Bieler A. et al., 2015, A&A, 583, A7
Biver N. et al., 2015, A&A, 583, A3
Bockelee-Morvan M. et al., 2015, A&A, 583, A6
Brin D., Mendis D. A., 1979, ApJ, 229, 402
Cave H. M., Tseng K.-C., Wu J.-S., Jermy, M. C., Huang, J.-C., Krumdieck, S. P., 2008, J. Comput. Phys., 227, 6249
Cowan J. J., A'Hearn M. F., 1979, Moon Planets, 21, 155
de Almeida A. A., Boczko R., Sanzovo G. C., Trevisan Sanzovo D., 2009, Adv. Space Res., 44, 335
El-Maarry M. et al., 2016, A&A, in press
Finklenburg S., Thomas N., Su C.-C., Wu J.-S., 2014, Icarus, 236, 9
Fulle M. et al., 2010, A&A, 522, A63
Fulle M. et al., 2016, ApJ, 821, 19
Haessig M. et al., 2015, Science, 347, aaa0276-1
Hirabayashi M., Scheeres D. J., Chesley S. R., 2016, Nature, 543, 352
Houpis H. L., Mendis D. A., Ip W.-H., 1985, ApJ, 295, 654
Ip W.-H. et al., 2016, A&A, in press
Jewitt D. C., 2004, in Festou M.C., Keller H.U., Weaver H.A., eds, Comets II. University of Arizona Press, Tucson, p. 659
Jorda L. et al., 2016, Icarus, 277, 257
Keller H. U. et al., 2007, Space Sci. Rev., 128, 433
Keller H. U. et al., 2015, A&A, 583, A34
Lai I.-L., Su C. C., Ip W.-H., Wei C.-E., Wu J.-S., Lo M.-C., Liao Y., Thomas N., 2016, Earth Moon Planets, 117, 23
Lara L. M. et al., 2015, A&A, 583, A9
Lee J.-C. et al., 2016, MNRAS, in press
Liao Y. et al., 2016, Earth Moon Planets, 117, 41
Lin Z.-Y. et al., 2015, A&A, 583, A11
Lin Z.-Y. et al., 2016, A&A, 588, L3
Lo M.-C., Su C.-C., Wu J.-S., Tseng K.-C., 2015, Comput. Phys. Commun., 18, 1095
Marschall R. et al., 2016, A&A, 589, A90
Moehlmann D., 1994, Planet. Space Sci., 42, 933
Pajola, M.et al., 2015, A&A, 583, A37
Schloerb P. et al., 2015, A&A, 583, A29
Sekanina Z., 1988, AJ, 95, 911
Sekanina Z., 1992, Asteroids, Comets, Meteors 1991. p. 545
Sekanina Z., 2008, in Hoover R.B., Levin G.V., Rozanov A.Y., Paul C.W., Davies P.C.W., eds, Proc. SPIE Conf. Ser. Vol. 7097, Instruments, Methods, and Missions for Astrobiology XI. SPIE, Bellingham, p. 15
Sierks H. et al., 2015, Science, 347, aaa1044
Steckloff J. K., Jacobson S. A., 2016, Icarus, 264, 160
Steckloff J. K., Johnson B. C., Bowling T., Jay Melosh H., Minton D., Lisse C. M., Battams K., 2015, Icarus, 258, 430
Su C. C. et al., 2010, Comput. Fluids, 39, 1136
Tenishev V., Combi M. R., Rubin M., 2011, ApJ, 732, 17
Thomas N. et al., 2015, A&A, 583, A17
Vincent J.-B. et al., 2015, Nature, 523, 63
Vincent J.-B. et al., 2016, MNRAS, in press
Weissman P. R., Kieffer H. H., 1982, Icarus, 52, 206
Wu J. S., Tseng K. C., Wu F. Y., 2004, Comput. Phys. Commun., 162, 166

[1]*Institute of Space Sciences, National Central University, No. 300, Zhongda Rd., Taoyuan City 32001, Taiwan*

[2]*Institute of Astronomy, National Central University, No. 300, Zhongda Rd., Taoyuan City 32001, Taiwan*

[3]*Space Science Institute, Macau University of Science and Technology, Taipa, Macau*

[4]*Department of Mechanical Engineering, National Chiao-Tung University, No. 1001 University Road, Hsinchu City 300, Taiwan*

[5]*Department of Earth Sciences, National Central University, No. 300, Zhongda Rd., Taoyuan City 32001, Taiwan*

[6]*Physikalisches Institut der Universität Bern, Sidlerstr 5, CH-3012 Bern, Switzerland*

[7]*Max-Planck-Institut für Sonnensystemforschung, Justus-von-Liebig-Weg 3, D-37077 Göttingen, Germany*

[8]*Department of Physics and Astronomy, University of Padova, Vicolo dell'Osservatorio 3, I-35122 Padova, Italy*

[9]*LAM (Laboratoire d'Astrophysique de Marseille), CNRS, Aix Marseille Université, UMR 7326, 38 rue Frédéric Joliot-Curie, F-13388 Marseille, France*

[10]*Centro de Astrobiologia, CSIC-INTA, E-28850 Torrejon de Ardoz, Madrid, Spain*

[11]*International Space Science Institute, Hallerstraße 6, CH-3012 Bern, Switzerland*

[12]*Scientific Support Office, European Space Research and Technology Centre/ESA, Keplerlaan 1, Postbus 299, NL-2201 AZ Noordwijk ZH, the Netherlands*

[13]*Department of Physics and Astronomy, Uppsala University, Box 516, SE-75120 Uppsala, Sweden*

[14]*PAS Space Research Center, Bartycka 18A, PL-00716 Warszawa, Poland*

[15]*Institut für Geophysik und extraterrestrische Physik (IGEP), Technische Universität Braunschweig, Mendelssohnstr 3, D-38106 Braunschweig, Germany*

[16]*Department of Astronomy, University of Maryland, College Park, MD 20742-2421, USA*

[17]*Gauss Professor, Akademie der Wissenschaften zu Göttingen and Max-Planck-Institut für Sonnensystemforschung, Justus-von-Liebig-Weg 3, D-37077 Göttingen, Germany*

[18]*LESIA-Observatoire de Paris, CNRS, Université Pierre et Marie Curie, Universite Paris Diderot, 5 place J. Janssen, F-92195 Meudon, France*

[19]*CNR-IFN UOS Padova LUXOR, Via Trasea, 7, I-35131 Padova, Italy*

[20]*Center of Studies and Activities for Space G. Colombo, CISAS, 'G. Colombo', University of Padova, Padova, Italy*

[21]*INAF, Osservatorio Astronomico di Padova, Vicolo dell'Osservatorio 5, I-35122 Padova, Italy*

[22]*Department of Physics and Astronomy, Uppsala University, Box 516, SE-75120 Uppsala, Sweden*

[23]*Department of Industrial Engineering, University of Padova, via Venezia 1, I-35131 Padova, Italy*

[24]*University of Trento, Via Mesiano 77, I-38100 Trento, Italy*

[25]*INAF – Osservatorio Astronomico, Via Tiepolo 11, I-34014 Trieste, Italy*

[26]*Instituto de Astrofísica de Andalucía (CSIC), Glorieta de la Astronomìa, E-18008 Granada, Spain*

[27]*Deutsches Zentrum für Luft- und Raumfahrt (DLR), Institut für Planetenforschung, Rutherfordstraße 2, D-12489 Berlin, Germany*

[28]*Operations Department, European Space Astronomy Centre/ESA, P.O. Box 78, E-28691 Villanueva de la Canada, Madrid, Spain*

[29]*Department of Information Engineering, University of Padova, Via Gradenigo 6/B, I-35131 Padova, Italy*

This paper has been typeset from a TEX/LATEX file prepared by the author.